

Relationships Between L-Band Brightness Temperature, Backscatter, and Physical Properties of the Ross Ice Shelf Antarctica

Kenneth C. Jezek¹, Shujie Wang, Marion Leduc-Leballeur², Joel T. Johnson¹, *Fellow, IEEE*,
 Marco Brogioni³, *Member, IEEE*, Julie Z. Miller⁴, David G. Long⁵, *Fellow, IEEE*,
 and Giovanni Macelloni⁶, *Senior Member, IEEE*

Abstract—Radiometric and radar data from NASA’s Soil Moisture Active Passive (SMAP) satellite are presented in a study of the Ross ice shelf, Antarctica. L-band brightness temperature (T_B) patterns compare favorably to the outflow patterns from East and West Antarctica. Cooler T_B is associated with the broad outflow from West Antarctic ice streams and the outflow from narrow outlet glaciers that drain East Antarctica. Aside from outlet glacier discharges, ice from East Antarctica is thinner and radiometrically warmer than that from West Antarctica. T_B is stable across the ice shelf over the 6-year period of observations (1–2 K standard deviation). Over shorter times, surface melt events cause pre- and post-melt T_B to vary by as much as 5 K in vertical polarization. Radar measurements highlight areas where backscatter is strong from melt-related ice lenses and ice layers, consistent with a corresponding decrease in T_B . The T_B polarization ratio on the ice shelf is approximately 1.13 and decreases from the West Antarctic grounding line toward the East Antarctic outlet glaciers. The backscatter polarization ratio increases by several dB from West to East Antarctica, indicating a decreasing influence of volume scatter toward East Antarctica. The decreasing T_B polarization ratio indicates a diminishing role of firn layering on the depth-integrated emission. There is a negative correlation between warming brightness temperature and thinning. An explanation for this observation is that the relatively warm ice shelf has a relatively shallow (500 m or less) penetration depth leading to a warm physical temperature bias.

Index Terms—Earth observations, microwave radiometry.

I. INTRODUCTION

ICE shelves exert important controls on the flow of inland ice sheets. Shear stresses along the margins of the ice shelf combined with longitudinal and shear stresses developed at ice rises result in buttressing forces that constrain the flow of the inland ice to the sea [1]. Removing an ice shelf would result in acceleration and thinning of the grounded inland ice causing an increased outward flux of ice and inevitably a contribution to sea level rise [2]. In the case of the Ross ice shelf (RIS), restraints on West Antarctic ice stream (WAIS) flow are particularly important because the gentle basal slopes and depression of the ice sheet base below sea level in this region promote instabilities that could cause the rapid retreat of the inland ice [3].

Systematic studies of the glaciology and geophysics of the RIS began during the 1957–1958 International Geophysical Year. The borehole at Little America V (LAV) was the first to penetrate through the column to provide estimates of ice temperature [4]. The RIS Project (RISP) and the RIS Geophysical and Glaciological Survey (RIGGS) [5] of the 1970s carried out a more extensive in situ and airborne measurement campaign that captured new information about ice motion, ice thickness, surface topography, basal topography, and geology. In addition, a borehole through the ice was completed in the southeastern quadrant of the ice shelf at RISP station J9 located east of Crary Ice Rise [6] (Fig. 1). In 2017, hot water drilling at two sites on the RIS studied the sub-ice water column [7]. The ROSETTA project [8] is the most recent survey of the ice shelf, and important results include new estimates of locations where melting and freezing are occurring at the base of the ice shelf.

As with other sectors of the ice sheet, spaceborne observations contribute much to our current knowledge about the RIS. Interferometric Synthetic Aperture Radar (InSAR) reveals the details of ice shelf surface motion [12] and the position of the ice shelf grounding line [13]. Surface elevation change measured by space-borne altimeters and mass change rates from spaceborne gravimeters are used to infer ice shelf mass balance [14]. Passive microwave brightness temperature and active radar backscatter data are essential for detecting surface melt [15], [16]. More recently, low-frequency microwave emission data are being used to explore

Manuscript received 29 August 2022; revised 24 October 2022; accepted 28 October 2022. Date of publication 1 November 2022; date of current version 15 November 2022. This work was supported in part by the National Aeronautics and Space Administration (NASA) Cryospheric Science Program under Grant 80NSSC18K0550, Grant 80NSSC22K0384, and Grant NNX14AH91G; and in part by the National Science Foundation under Grant 1838401. The work of Marion Leduc-Leballeur, Marco Brogioni, and Giovanni Macelloni was supported by the Italian Space Agency (ASI) Project Cryorad Follow-On under Contract 2021-1-U.O. (*Corresponding author: Kenneth C. Jezek.*)

Kenneth C. Jezek is with the Byrd Polar and Climate Research Center, The Ohio State University, Columbus, OH 43210 USA (e-mail: jezek15@gmail.com).

Shujie Wang is with the Department of Geography and Earth and Environmental Systems Institute, Pennsylvania State University, University Park, PA 16802 USA (e-mail: skw5660@psu.edu).

Marion Leduc-Leballeur, Marco Brogioni, and Giovanni Macelloni are with the Institute of Applied Physics “Nello Carrara” of the National Research Council, 50019 Sesto Fiorentino, Italy (e-mail: m.leduc@ifac.cnr.it; m.brogioni@ifac.cnr.it; g.macelloni@ifac.cnr.it).

Joel T. Johnson is with the ElectroScience Laboratory, The Ohio State University, Columbus, OH 43210 USA (e-mail: johnson.1374@osu.edu).

Julie Z. Miller is with the Earth Observations, Cooperative Institute for Research in Environmental Sciences, Boulder, CO 80309 USA (e-mail: jzmiller.research@gmail.com).

David G. Long is with the Department of Electrical and Computer Engineering, Brigham Young University, Provo, UT 84602 USA.

Digital Object Identifier 10.1109/TGRS.2022.3218538

the grounded portion of the ice sheet by relying on the lower rate of absorption and hence deeper penetration into glacial ice. NASA's Soil Moisture Active Passive (SMAP) and ESA Soil Moisture Ocean Salinity (SMOS) satellite data have been used to study intraglacial ice temperature across the interior ice sheet [17], [18] and to detect surface melt [19] and firn aquifers in the peripheral areas of Greenland [20], [21] and Antarctica [22]. These studies illustrate the potential for understanding the ice thermal state from the surface to the base and motivated additional studies using ultra-wideband radiometers (0.5–2 GHz), albeit operated over more geographically limited sectors of the ice sheets [23], [24], [25], [26]. Applications of radiometrically derived temperatures from aircraft to infer ice rheology parameters were recently further investigated by Jezek et al. [27].

Here we describe an initial investigation of L-band SMAP radiometric and radar observations for monitoring ice shelf properties. We use SMAP radar data to distinguish regions where brightness temperature is impacted by the near surface from those where the microwave emission is sensitive to the deeper volume of the ice shelf. We further compare RIS brightness temperature and radar backscatter patterns to glaciological parameters such as surface melt/freeze, ice temperature, and ice thickness to gain further insight into the use of SMAP data for ice shelf sensing.

II. SMAP INSTRUMENTS

The SMAP mission was launched in January 2015 and began operations in April 2015 [28]. The mission was placed in a sun-synchronous circular polar orbit with an 8-day repeating ground track. There are both a radar and a radiometer on board the satellite. The radiometer measures thermal radiation at 1.41 GHz in horizontal (H), vertical (V), and the 3rd and 4th Stokes polarizations. The radar operates at 1.26 GHz and measures VV, HH, HV, and VH polarized backscatter. Unfortunately, the radar stopped transmitting on July 7, 2015, as a result of an anomaly involving the high-power amplifier. (The microwave radiometer was unaffected by the anomaly.) Mission objectives focus on measuring global soil moisture and soil freeze/thaw state from space. Though not specifically designed for broader studies of the cryosphere, the SMAP operating frequency and polarization attributes are well suited for studies of polar ice because the low electromagnetic absorption rate of glacier ice in the 1–1.4-GHz range allows the sensor to probe the depths of the ice.

The nominal radiometer spatial resolution is 39×47 km and the brightness temperature accuracy is quoted as 1.3 K for the standard 36-km products. The instrument's look angle is 40° . The large field of view means that the surface brightness temperature overlaps between adjacent footprints and overlapping swaths. This allows improved resolution to be obtained after the application of the radiometer version (rSIR) of the scatterometer image reconstruction (SIR) algorithm [29], [30]. Combined with the irregular pattern of measurement locations, the 36-km standard grid data can be reconstructed onto a 3.125-km grid which are the data used in this analysis [31]. The effective spatial resolution of this

product is ~ 18 km and the brightness temperature accuracy remains about 1.3 K.

The SMAP radar collected “footprint” (29×35 km) and “slice” (6×30 km) backscatter data globally and synthetic aperture radar (SAR) data over most land areas [32]. Unfortunately, SAR data were not collected over Antarctica. As with the radiometer data, the overlap between adjacent footprints and swaths can be exploited to enhance the spatial resolution of the slice measurements using the scatterometer form of the SIR technique to a 3.125-km grid [33], [34] with an effective resolution of 5–10 km. As seen in previous scatterometer missions [35], [36], SMAP backscatter measurements over ice sheets exhibit azimuthal variations due to wind-formed sastrugi and other features. Corrections for azimuth and incidence angle are applied to the images used in this article [37]. The 3.125-km grid size used for the radiometer and radar images is an integer (8) divisor of the 25-km base grid of the EASE-Grid 2.0 map projection [38], [39] used and ensures that the Nyquist sampling criterion is met in reconstruction processing.

III. ICE SHELF PHYSICAL PARAMETERS AND MICROWAVE PROPAGATION

The RIS with an area of about 5×10^6 km² is a slab of floating snow and glacial ice separating portions of East and West Antarctica and bounded to the north by the Ross Sea (Fig. 1). Ice over 800-m thick is found near the grounding line that then thins to less than 200 m at the terminus. One side of the ice shelf is fed by WAISs, while the other is fed by outlet glaciers that pierce the Transantarctic Mountains. Meteoric ice deposited on the surface and, in some places marine ice accreted to the base, also modify the ice shelf composition. The past and present motion of the ice shelf is governed by dynamic forcings characteristic of differences between the inland ice sheets, stresses within the ice shelf, interaction with the margins and ice rises, and atmospheric and oceanographic transport processes that control ocean heat flux, surface accumulation, and basal melt.

Here, we briefly summarize the properties of the RIS most relevant to the interpretation of the SMAP data. Ice thickness patterns compiled by the earlier Bedmap2 [9] and the later BedMachine 2 [10] are shown in Fig. 1. The general features compare favorably with the thickness map compiled from 1970's surface and airborne data [40]. Notable is the complex pattern of thickness variations reflecting ice-shelf dynamics. Thick, broad lobes of ice extend outward from the WAISs toward the 180° meridian. These range from about 900-m thickness near the grounding line to about 400 m after several hundred kilometers of transport where patterns diffuse into the background. The character of the thickness changes roughly west of the 180° meridian where narrow ribbons of thicker ice reach into the RIS from the East Antarctic outlet glaciers, most notably from Byrd Glacier (BG).

At the surface, snow accumulation and mean annual temperature impose boundary conditions on the physical temperature profile and hence T_B . Annual surface accumulation patterns appear as a central plume of 80–100 mm/yr of

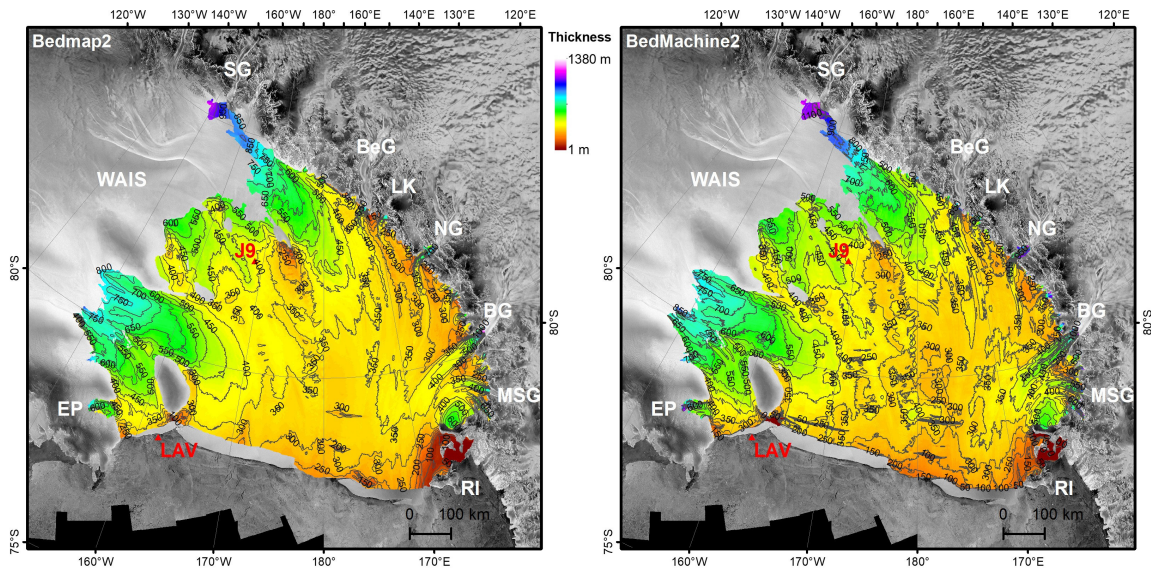


Fig. 1. (Left) RIS ice thickness maps from BedMap2 [9] and (Right) BedMachine 2 [10] overlaid on a C-band Radarsat backscatter image. Ice thickness is 412 ± 134 m on average (BedMachine v2). The contour interval is 50 m. Locations of RIGGS station J9 and LAV are also shown. Glacier systems include: the WAISs; SG; Beardmore Glacier (BeG); LKG; Nimrod Glacier (NG); BG; and MSG. The Edward VII Peninsula (EP) and RI are also shown. The base map is a product of the Radarsat Antarctic Mapping Project [11]. This and later maps are displayed on a polar stereographic projection.

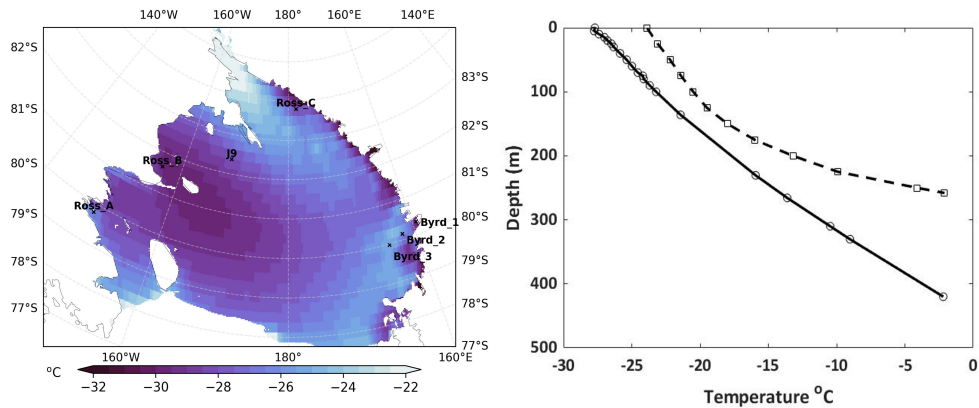


Fig. 2. (Left) 6-year average ERA5 skin temperature from September 2015 to August 2021 over RIS. (Right) Borehole measured physical temperature at LAV [41] (dashed) and J9 (solid) [6] on the RIS. Markers show the depths at which temperature was measured.

water equivalent extending southwest across the central shelf and flanked by higher accumulation bands up to 240 mm/yr along the Transantarctic Mountains and Roosevelt island [42]. Reported 10-m temperatures have a similar spatial pattern, but the maximum range of temperatures is -23 °C to -28 °C which are further limited to about -25 °C to -28 °C over most of the central ice shelf [42], [43]. Fig. 2 shows the mean ECMWF Reanalysis v5 (ERA5) skin temperature between September 2015 and August 2021. The mean value skin temperature (-27.30 °C \pm 1.75 °C) is slightly cooler than 10-m depth temperatures [42]. The low standard deviation (SD) of the skin temperatures over the observation period demonstrates that surface temperatures are stable over the ice shelf.

The volume of the ice shelf is not homogeneous and disrupts upwelling radiation. Crevasses and rifts fracture the surface to tens of meters depth and scatter microwave radiation. Flanking

the outflow from East Antarctic glaciers are absorptive bands of brine and scattering debris scraped from the sides of the outlet glacier walls [44]. These are traceable down the length of the ice shelf. Similar phenomena were observed downstream of the Crary ice rise [45]. A unique feature of ice shelves is sea-water-filled bottom crevasses. At station J9, the crevasses penetrate into the base up to 120 m and are tens of meters wide, and have periodicities of several hundreds of meters [46]. Additional zones of bottom crevasses that fracture up to 75% of the total ice thickness were mapped in the eastern sector of the ice shelf but are also present near the grounding line of Transantarctic mountain outlet glaciers. Bottom crevasses tend to refreeze as they migrate downstream. The local effect of the crevasses on the temperature profile and bulk dielectric properties remains undetermined.

Borehole measurements of ice shelf temperature profiles were acquired at two sites (Fig. 2, right). The 1958 drill

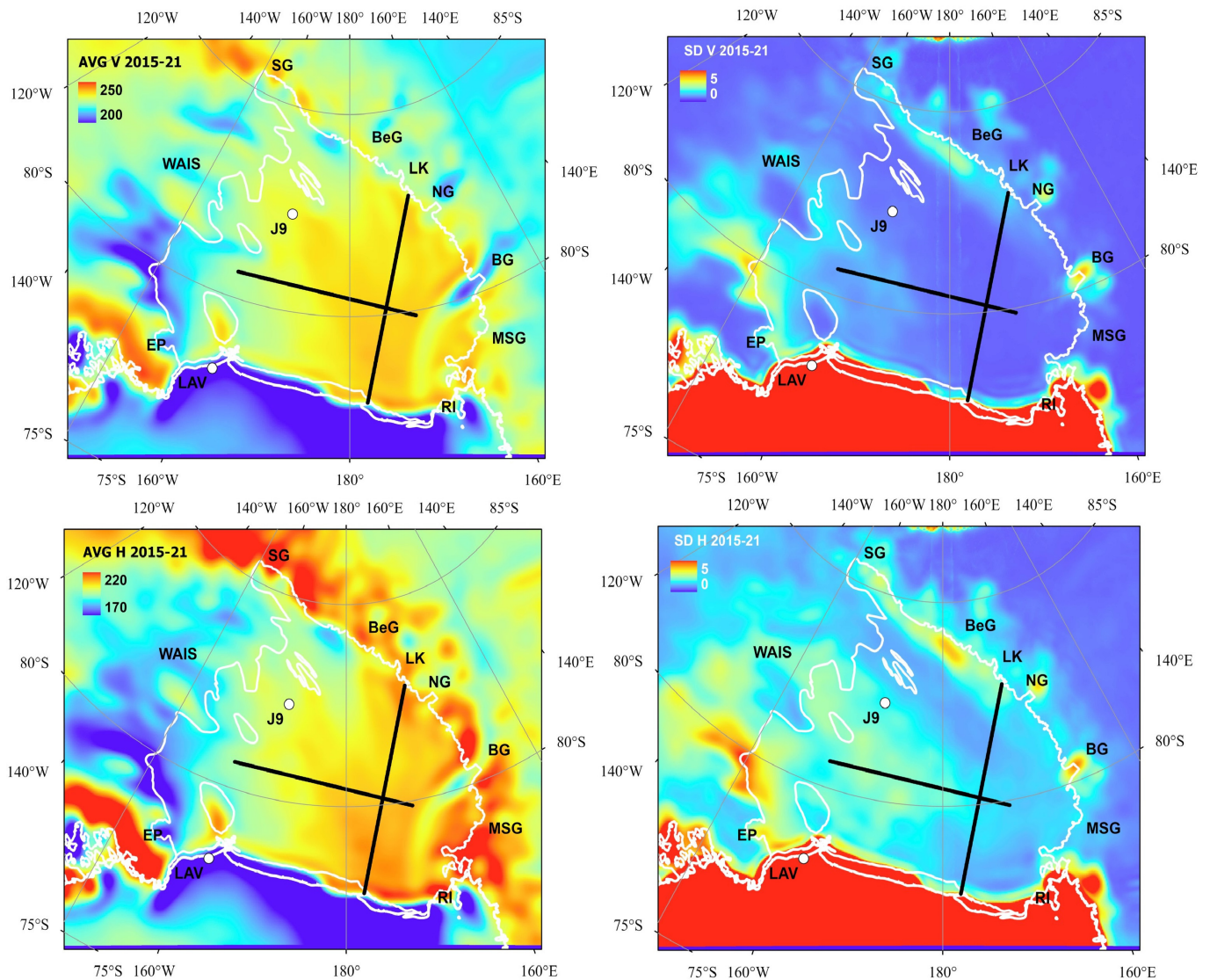


Fig. 3. (Top left) Vertically polarized SMAP brightness temperature averaged over 2015–2021 and (Top right) SD of the brightness temperature over the same period. (Bottom left) Polarized SMAP brightness temperature averaged over 2015–2021 and (Bottom right) SD brightness temperature over the same period [29], [39]. Two profile lines are shown. Profile 1 trends laterally across the ice shelf and was selected to avoid regions where substantial melt occurred and to avoid the outflow of BG. Profile 2 runs longitudinally from the terminus to LKG. High and low parameter values are given in the legend.

site at LAV was at the time of measurement located about 3 km upstream from the ice front at an elevation of 43 m (Fig. 1). Pit and ice core analyses show evidence for surface melt resulting in ice layers and ice lenses along with the development of depth hoar layers [41], [47]. Temperatures gradually increase with depth to the melting point at the base [48]. The energy balance results in basal melt estimated at about 0.6 m/yr [49]. Temperatures at LAV are typical of an ice column where the vertical and horizontal advection of cold ice reduces the temperature gradient in the upper column before heat conduction becomes dominant as the ice warms to the base.

Station J9, located about 70 km northwest of Crary Ice Rise, is situated in the outflow of the more southerly WAISs (Fig. 1). Borehole temperature was measured to a depth of 330 m and extrapolated to the sea water temperature at the

base [6], [50], [51]. The temperature at J9 varies almost linearly with depth. The behavior was explained by MacAyeal and Thomas [52] by modeling the very slow accretion of 6 m of marine ice to the base of the ice column [53]. Although temperature data were collected more than 60 years ago (these are the only available), they are considered representative of current RIS conditions.

Along with observations of a basal saline ice layer at J9, Jezek [45] estimated basal freeze-on rates between 22 and 34 ± 7 cm/yr in a flow band extending downstream from Crary Ice Rise. A thin (10 cm) layer of ice crystals was observed in oblique photographs of the ice bottom by Stevens et al. [7] at a drill site located about 300 km from the ice shelf front ($80^{\circ}39.5' S$, $174^{\circ}27.7' E$). They concluded that any marine ice at this location is ephemeral. Patterns of basal melt and refreeze were inferred by Das et al. [8] and Moholdt et al. [54]

who find irregular and weak patterns of melt and freeze on the central ice shelf. They found more uniform areas of basal melt along the terminus and also with the landward portion of East Antarctic Ice Sheet (EAIS) outlet glaciers.

IV. RADIOMETRIC MEASUREMENTS OF THE RIS

Enhanced resolution SMAP vertical (T_B^v) and horizontal polarization (T_B^h) brightness temperature maps across the RIS averaged over all data from 2015 to 2021 are shown in Fig. 3 [29]. The SD maps computed from daily T_B measurements over the same 6-year time period are also shown. Brightness temperatures are warmest in the western ice shelf and approach 250 K for T_B^v and 235 K for T_B^h along the terminus near Ross Island (RI) where Das et al. [8] estimated basal melt rates in excess of 2 m/yr. Warmer T_B s are generally associated with the outflow roughly west of the 180° meridian and originating from East Antarctica. There the ice (Fig. 1) will be on average warmer with depth because the conduction gradients increase through the thinner ice and given the more or less fixed temperatures at the surface and base. T_B cools in the east due to the thicker ice plumes descending from the WAISs. T_B s are the coolest near the Edward VII Peninsula (EP) where they fall as low as 190 and 160 K for T_B^v and T_B^h respectively. As discussed later, this corresponds to an area where surface melt episodically occurs. Scattering from icy bodies and reduced transmission from ice layers formed during surface melt can cool T_B by tens of kelvin at L-band relative to melt-free regions [55].

Cool T_B is also associated with the cold flow from outlet glaciers that breach the Transantarctic Mountains from Scott Glacier (SG) to Mullock/Skelton Glacier (MSG). The outflow from BG is indicated by a prominent T_B signature that extends from the grounding line nearly to the ice shelf terminus. A combination of factors may be responsible for preserving the outlet glacier signature on the ice shelf including the downslope flow of cold air from the plateau and scattering from crevasse fields carried downstream with the flow. Cold outlet glacier T_B is also associated with regions where strong basal melting is reported near the grounding lines [54].

Brightness temperatures for both polarizations are very stable over the period of observations as illustrated by the SD of measurements over the 6-year observation period. The SD in brightness temperature over the ice shelf is 1.0 K for T_B^v and 1.9 K for T_B^h on average. Larger variations are notable along the margin of the ice shelf from SG to MSG where the SD can be >5 K because adjacent mountainous topography introduces additional variability during the image reconstruction processing. Temporally stable SMAP brightness temperatures and deep penetration depth in the shelf ice imply that short-term meteorological processes are mitigated in the multiyear average signal. The relatively stable glaciological setting and long-term data record over RIS, therefore, make the RIS an ideal site to link microwave radiometry and radar with various field, airborne, and spaceborne data sets.

The T_B^v/T_B^h polarization ratio is shown in Fig. 4. Within the ice shelf the ratio is on average about 1.13 but there is

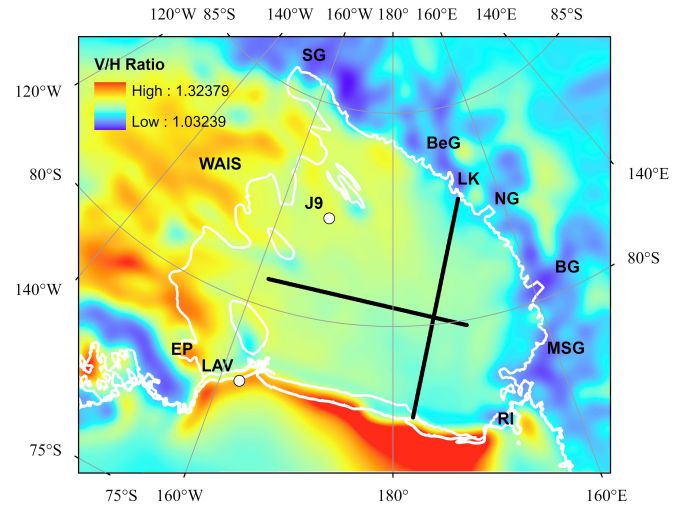


Fig. 4. T_B^v/T_B^h ratio calculated using the 6-years average SMAP T_B . Straight black lines are profile transects investigated for detailed analyses.

a gradual eastward reduction of the ratio that appears to be related to ice source regions spanning West Antarctica (high polarization ratio of about 1.3) to East Antarctica (low ratio approaching unity). It is worth noting (but somewhat beyond the scope of this article) that large changes in polarization ratio appear to be associated with the West Antarctic grounding line and perhaps the grounding line along the Transantarctic Mountains, although terrain features may bias the results in this region. Exceptions are BG (for which the polarization signature upstream carries only a small distance onto the ice shelf) and also along the Edward VI peninsula (EP).

A. Surface Melt on the RIS

Major surface melt events across the RIS are episodic and correspond to an increase in T_B . Refreezing reduces T_B through the formation of scattering ice bodies which, as they are buried by snow accumulation, cause T_B to increase slowly with time to a stable pre-melt value. Similar scattering layers are observed across the dry snow facies of the Greenland ice sheet, resulting in similar L-band signatures [56]. Two particularly strong surface melt events occurred in early 2016 and 2017. Using a melt detection algorithm [57] applied to 19-GHz Advanced Microwave Scanning Radiometer (AMSR2) observations, Fig. 5 shows the annual melt distribution during the six seasons from 2015 to 2021. Surface melt is largely confined to the eastern portion of the ice shelf where warm air intrudes over the eastern edge of the ice shelf and pushes south and westward. The extensive surface melt event in January 2016 was linked to the strong advection of warm air from the ocean and was argued to be favored by the 2015–2016 El Niño event [58]. Also shown in Fig. 5 is the location of four sites on the ice shelf called Ross A (79.79°S, 149.59°W), B (81.64°S, 156.39°W), and C (83.80°S, 178.05°E), and RIGGS station J9 for which time series SMAP T_B are presented in Fig. 6. The particularly strong surface melt event in January 2016 is revealed at sample sites A and B

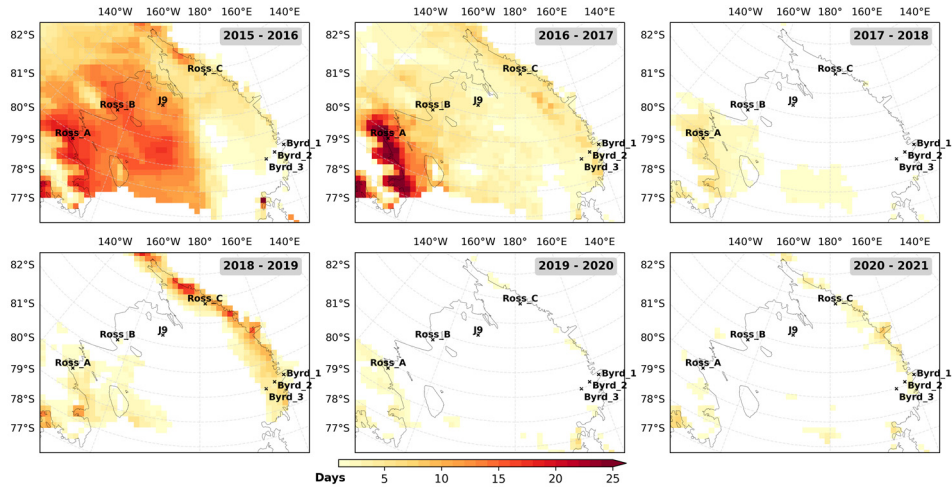


Fig. 5. Number of surface melting days detected by AMSR2 between September and June over RIS during the six seasons from 2015 to 2021. The named location of time series sample sites (Figs. 6 and 7) is indicated with black crosses.

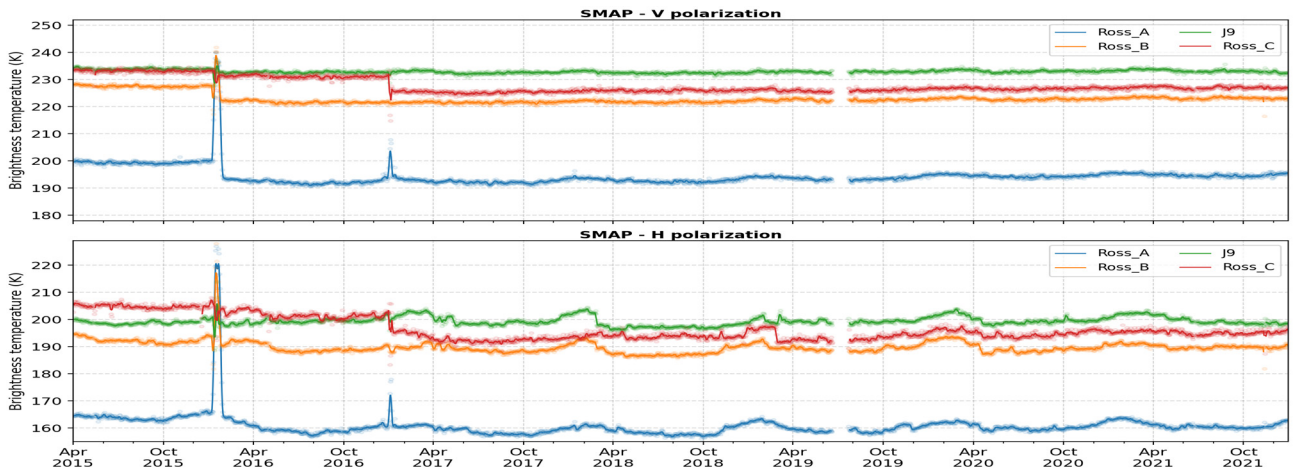


Fig. 6. Time series of SMAP (Top) vertical and (Bottom) horizontal polarized TB for the four sample sites closest to West Antarctica shown in Fig. 5. Surface melt events are indicated by the brief warming to near blackbody temperatures followed by an abrupt cooling of the emission.

by a brief strong increase in T_B indicative of melt followed by a ~ 6 K decrease in vertical polarization. Sites *A* and *C* show a subsequent event in 2017. Brightness temperatures gradually warm with time (about 2 K in 5 years in vertical polarization), suggesting that disturbances in the upper firn are buried by subsequent snow accumulation.

Fig. 5 also shows the location of three sites located in the outflow of BG. Byrd-3 is located downstream on the ice shelf. T_B^v varies negligibly whereas T_B^h varies by only a few Kelvin seasonally (Fig. 7). The stable signature implies that melt is absent at this location for the period of observations. Seasonal variations (up to 20 K) increase farther upstream perhaps associated with short-duration melt events enhanced by insolation reflected from the valley walls.

V. SMAP RADAR

SMAP radar data collected during the first 3 months of the system's operational period reveal important details for interpreting the T_B data. Fig. 8 shows vertically and horizontally

polarized backscatter maps adjusted for incidence and azimuth angle [37]. Tonal signatures on the ice shelf are generally slowly varying. Brighter signatures for both polarizations occur near EP and are in part associated with morphologic changes to the firn caused by prior surface melt events discussed above. The outflow of BG is also bright in part from crevasses carried downstream. Crevassing immediately downstream of the other outlet glaciers as well as immediately downstream of Cary Ice Rise also results in bright returns. The scattering edges of two long rifts orthogonal to flow are noticeable near 180° W longitude and 79° S latitude. The range of backscatter coefficients σ_0 is similar for both polarizations (-20 to -14 dB and -21 to -12 dB, respectively, in VV and HH polarizations).

The radar polarization ratio [taken in decibels as $10\log(\sigma_0^{vv}/\sigma_0^{hh})$] increases from east to west (Fig. 9). The ratio is smallest (about -2 dB) surrounding Roosevelt Island where, as has been mentioned, refrozen melt layers recent to the time of the radar data are likely increasing HH backscatter. The ratio increases to 1–2 dB farther west.

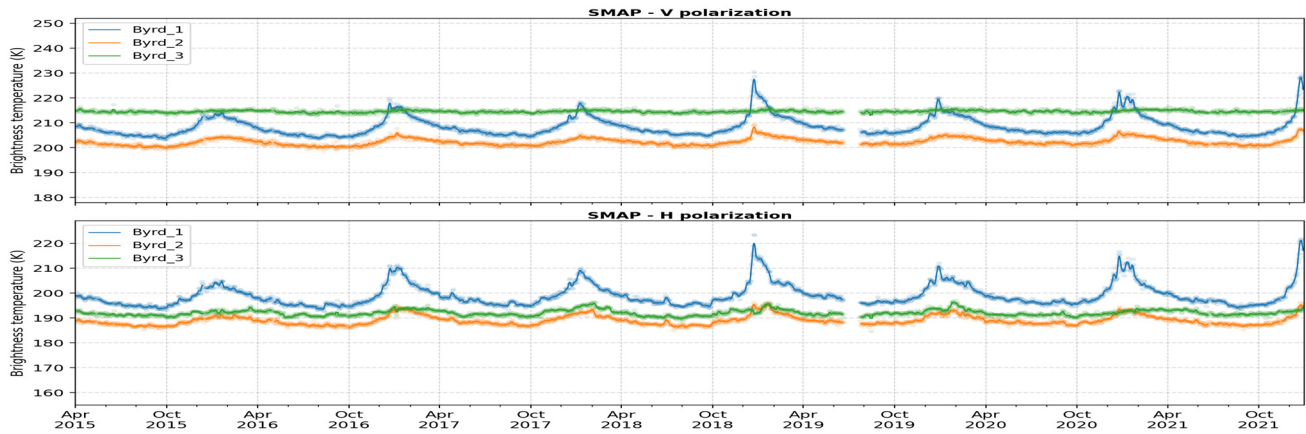


Fig. 7. Time series of SMAP (Top) vertical and (Bottom) horizontal polarized TB for the three sample sites near BG shown in Fig. 5.

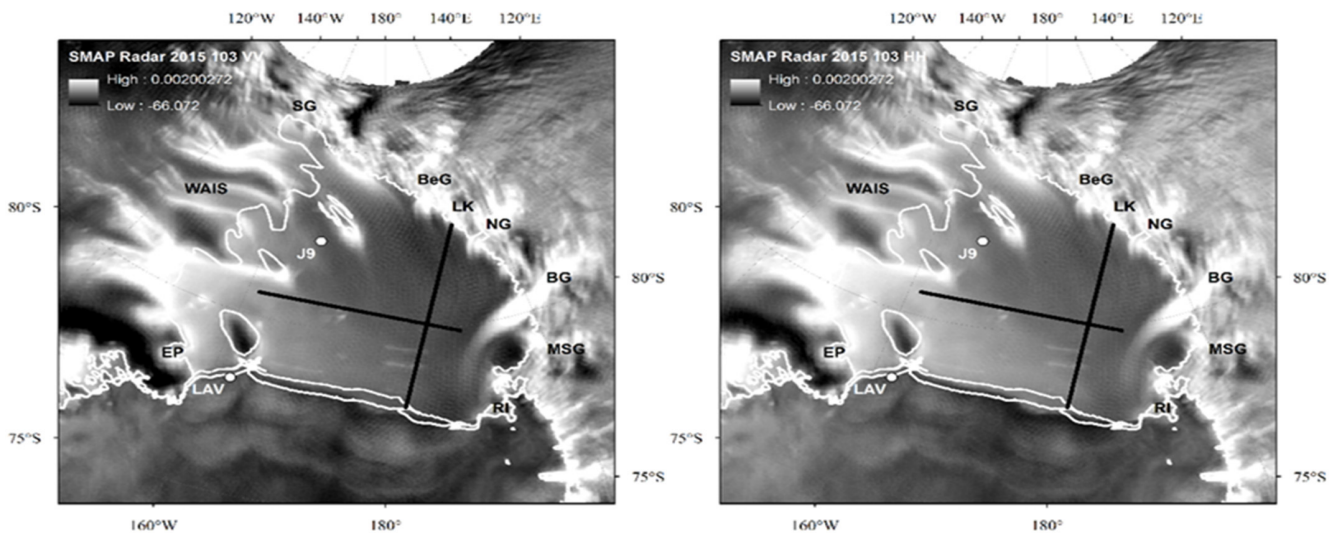


Fig. 8. SMAP radar backscatter maps (decibels) adjusted for incidence angle and azimuthal variations [37]. (Left) VV polarized. (Right) HH polarized. Straight black lines are profiles along which physical properties are collected.

The SMAP radar and radiometer data are compared along the two profile lines shown in Fig. 3. Profile 1 was selected roughly parallel to the terminus and across the central region of the ice shelf. The ice thickness gradients are the largest along this profile (Fig. 1). The profile spans the outflow from East and West Antarctica. The endpoints were selected to avoid major melt-related effects and also to avoid the outflow of BG. Profile 2 was selected outside the melt zone and extended from the terminus to the outflow of the Lennox King Glacier (LKG). Profile 2 is primarily situated in the outflow from East Antarctica.

The multiyear average brightness temperature and early mission backscatter coefficients along each line are shown in Figs. 10 and 11 along with scatter plots of the two parameters. For both polarizations, brightness temperature and backscatter are inversely correlated for profile 1, consistent with the results from Zeng et al. [59] who considered global data sets. In contrast to Zeng et al. [59], who found a low correlation in polar and arid regions, the Pearson correlation

coefficient (r) is about -0.95 when T_B is regressed against linear backscatter for both polarizations. Linear slopes fit to the data are -1.9 and -2.2 K/dB for vertical and horizontal polarization, respectively. The $2\text{--}3$ K decreasing difference between T_B^v and T_B^h along the profile results in the decreasing polarization ratio observable in Fig. 4. The VV-pol radar backscatter is about 2 dB less than the HH-pol data at the start of the profile, while the backscatter from each channel is the same near the midpoint, and VV-pol exceeds HH-pol by about 1 dB near the profile end. The dynamic range of the VV-pol radar data is about 3 dB narrower than the HH-pol.

The situation for profile 2 is different. Here, T_B^v and T_B^h are positive albeit weakly correlated with the respective radar channels (Pearson correlation coefficients of 0.6 and 0.4 for the vertical and horizontal channels, respectively, and a linear backscatter scale). Linear slopes fit to the data are 1.4 and 0.75 K/dB for the vertical and horizontal polarizations respectively. Zeng et al. [59] find that the correlation is poor in polar and arid regions due to several environmental

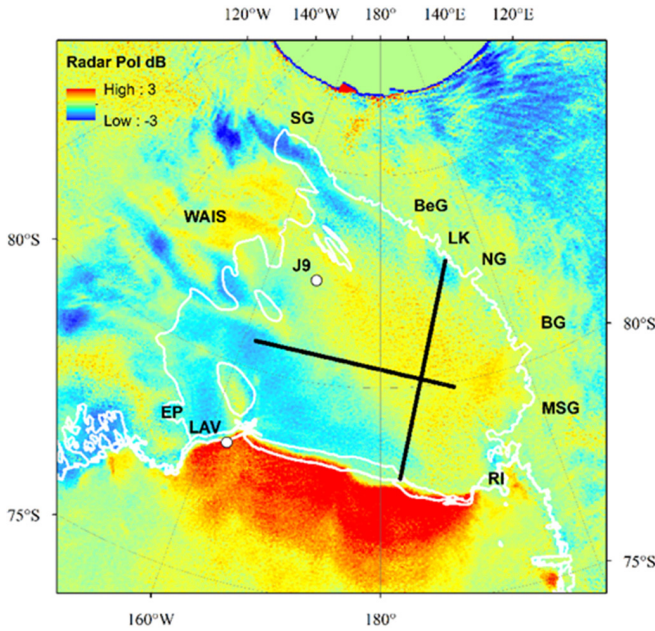


Fig. 9. VV/HH radar backscatter polarization ratio in decibels. Straight black lines are profiles investigated for detailed analyses.

factors including increased volume scattering and low physical temperature. For profile 2 there is an additional complication of changing glaciological conditions as the line proceeds from the terminus near the ocean, to the central RIS and finally to the Transantarctic Mountains. In detail, the along-track variations in T_B^v and T_B^h are similar at the start of the profile near the terminus, but the dip in T_B^h near the midpoint is more pronounced. For the radar, the two polarization channels are nearly identical at the start of the profile but the VV-pol increases by about 1 dB near the midpoint after which the difference diminishes near the outflow of LKG where scattering from crevasses increases the backscatter and dims the brightness temperature.

Some of the correlation may be due to modification of the firn due to melt in the east. There are several reasons to believe that other factors are at play. Observations in Greenland showed that there was about a 30 K difference in T_B for L-band, circular polarization, and normal incidence observations between regions where extensive surface melt modified the upper firn and where surface melt was largely absent [56]. Here, the difference between the pre- and post-melt vertically polarized T_B is only about 5 K (Fig. 6). Also, the brightness temperature data are averaged over several years which likely mutes melt-related effects. The contrasting correlations of backscatter and brightness temperature between profiles 1 and 2 also suggest additional mechanisms beyond melt are modifying the microwave signatures.

VI. CORRELATION BETWEEN SMAP AND ICE THICKNESS

Heat conduction through the ice is a major control of ice temperature gradients which are determined largely by ice thickness. Here, we investigate relationships between T_B and ice thickness as a proxy for temperature. SMAP T_B^v , T_B^h , and

ice thickness from BedMachine2 [10] are compared along the profiles in Figs. 12 and 13. The trends are inversely related, so warmer brightness temperatures are associated with thinner ice. Scatter plots for profile 1 show that brightness temperature becomes less sensitive for thicknesses greater than 500 m and where the profile line approaches the surface melt-event region. T_B is uncorrelated with a thickness of less than about 240 m along profile 2 near the terminus where proximity to the ocean may start to contaminate the T_B signature.

A similar functional relation between T_B and ice thickness is found for the entire spatial area of the ice shelf. Scatter plots for the vertical and horizontal polarized data are shown in Fig. 14 wherein all the ice shelf data are plotted and where the data are trimmed for thickness greater than 900 m. The fit lines have slopes similar to the profile data.

A second regression was computed for a 6-day period in April 2015 to avoid the effects on T_B from the 2016 melt event. With the empirical, functional relationship between T_B and ice thickness defined, it is possible to difference T_B computed using the empirical relationship with ice thickness and the measured T_B (Fig. 15). The upper portion of Fig. 15 shows the difference between the predicted T_B using the April 2015 regression and the measured April T_B . The lower figure shows the same regression formula differenced from the multiyear average T_B maps. The difference for both T_B^v and T_B^h is about ± 5 K in the central ice shelf. The largest negative departures in both polarizations occur along the flanks of the BG outflow. There are noticeable T_B^h anomalies associated with Nimrod, Lennox King, and Beardmore Shackleton glaciers draining East Antarctica. Negative anomalies imply an underestimate of the regression model T_B . Negative anomalies are more spatially extensive for horizontal polarization. This suggests that additional effects of spatially varying layering in the firn are not properly accounted for in the simple linear model. Strong positive anomalies that are more extensive in vertical polarization are correlated with outflow from the WAISs and BG. Increased volume scattering from refrozen ice lenses and crevasses in these areas causes the simple model to overpredict T_B .

VII. DISCUSSION

Previous results on the grounded ice sheet have argued that the 1.4 GHz T_B varies with ice thickness through the relationship between thickness and physical temperature [18], [25], [59]. For the ice shelf, upwelling emission from the ocean into the ice is relatively cold because the large dielectric contrast between ocean and ice severely limits transmission (about 55% transmission). There should also be less attenuation of the cold ocean emission traversing a thinner ice column. Moreover, the thinner the ice, the less ice there is available to emit. This suggests that thin ice should be radiometrically cold. However, the RIS observation is that thinner ice is radiometrically warmer, contrary to expectations based on observations of the inland ice sheet [18], [25], [60].

Additional factors can warm the near-basal emission and change the functional relationship between T_B and ice thickness. Basal melt/freeze patterns are influenced by the shape

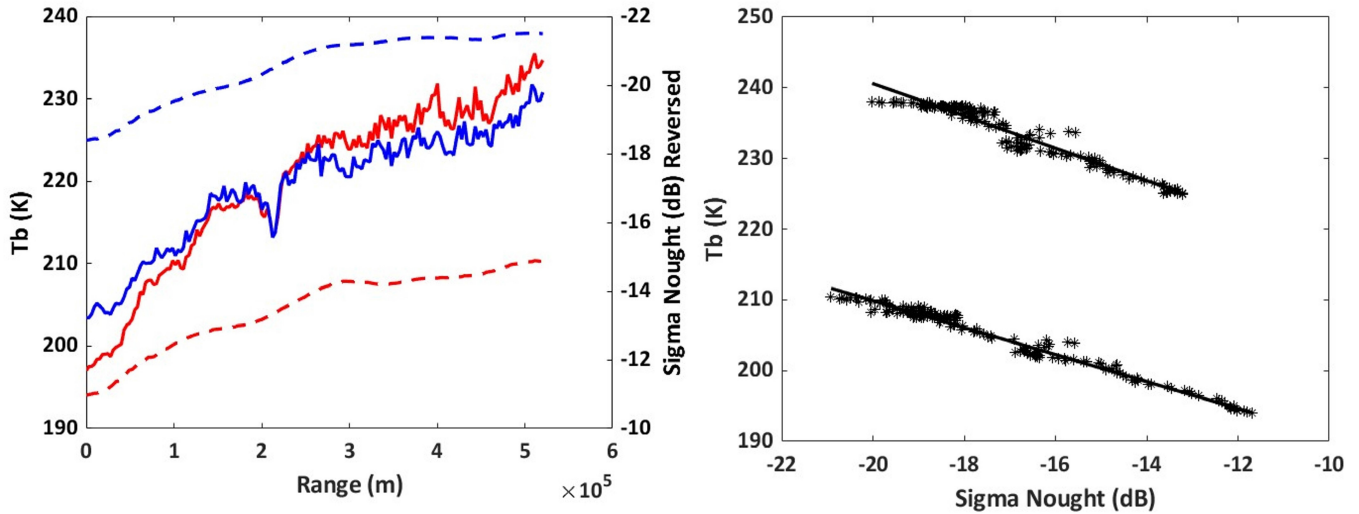


Fig. 10. (Left) Profiles of T_B^v (blue dashed), T_B^h (red dashed), and backscatter (blue VV-pol and red HH pol) are shown along the east/west profile. The horizontal axis is the range along the line direction. (Right) Scatter plots of T_B versus backscatter. Vertical polarization T_B data are warmer.

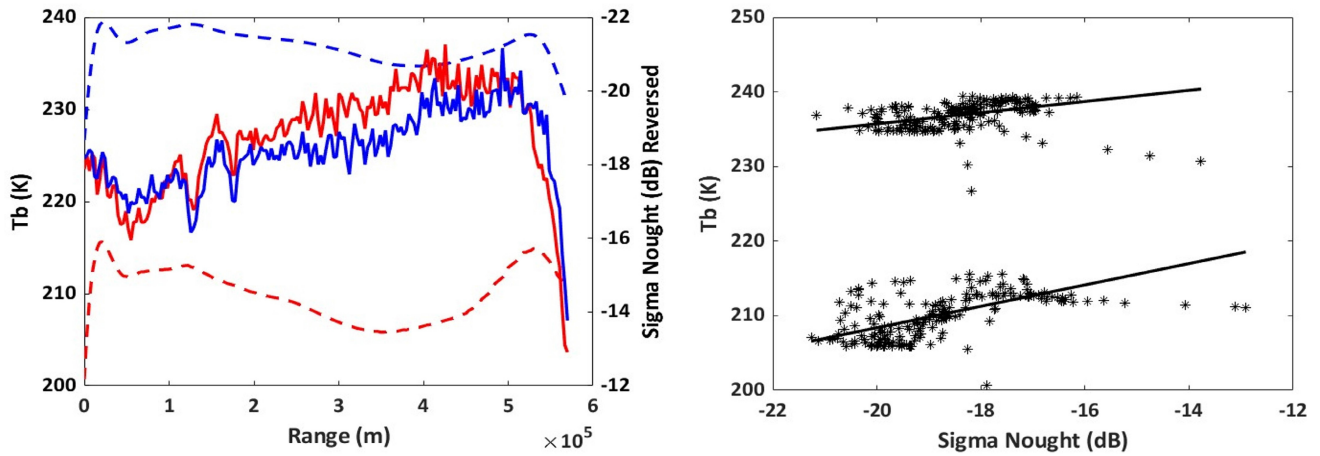


Fig. 11. (Left) Profiles of T_B^v (blue dashed blue), T_B^h (red dashed), and backscatter (blue VV-pol and red HH pol) are shown along the north/south line. The horizontal axis is the range along the line direction. (Right) Scatter plots of T_B versus backscatter. Vertical polarization T_B data are warmer. North/south scatter was fit to radar data less than -16 dB to avoid data near the grounding line of LKG.

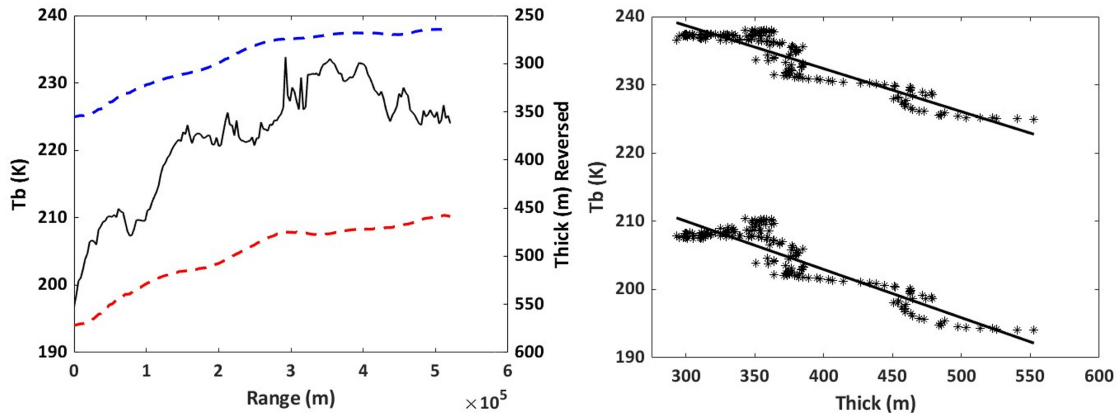


Fig. 12. (Left) Profiles of T_B^v (blue dashed), T_B^h (red dashed), and BedMachine 2 ice thickness (solid) along east to west profile line. Note that the right-hand scale on the profile plots assigns thickness increasing downward. The horizontal axis is range in meters along the profile. (Right) V-pol (warm) and H-pol (cool) scatter plots with linear regression.

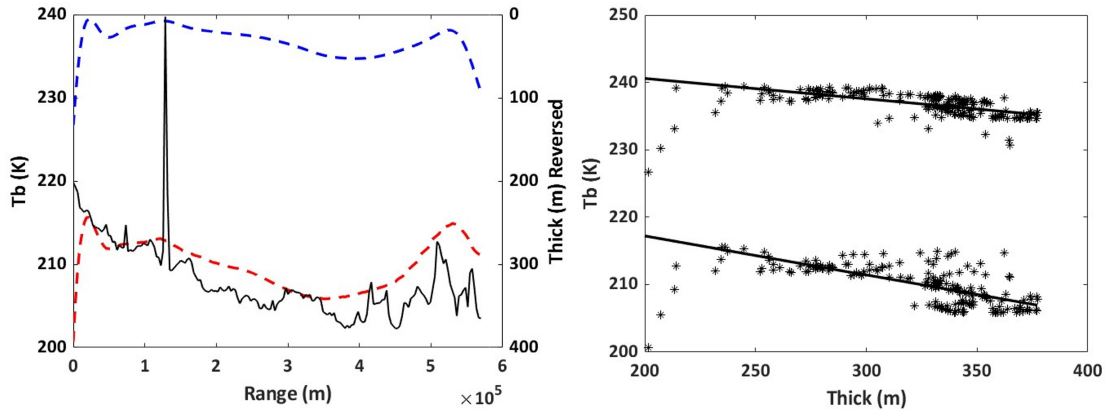


Fig. 13. (Left) Profiles of T_B^v (blue dashed), T_B^h (red dashed), and BedMachine 2 (solid) along the north-to-south line. The thickness spike is associated with a rift. Note that the right-hand scale on the profile plots assigns thickness increasing downward. The horizontal axis is the range along the profile in meters. (Right) V-pol (warm) and H-pol (cool) scatter plots with linear regression.

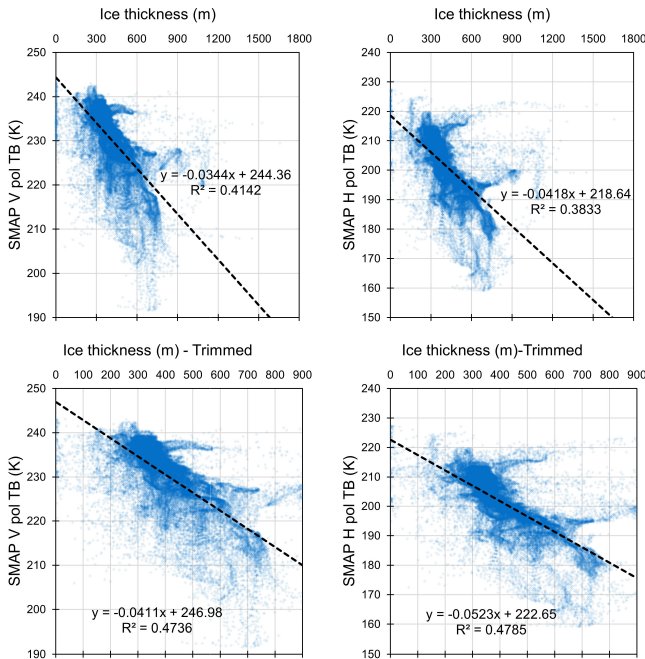


Fig. 14. (Top) Vertical and horizontal polarization scatter plots for all thickness and T_B data on the RIS; (Bottom) scatter plots trimmed to exclude thickness greater than 900 m.

of the oceanic cavity which is defined by ocean topography and ice thickness. Accretion of a warm saline ice layer to the base of the ice shelf increases T_B because absorption in the saline ice results in more emission that is less attenuated across the reduced dielectric contrast at the marine ice–glacier ice boundary. Radiative transfer modeled emission using the J9 temperature profile and a 6-m-thick marine ice layer (salinity 2–4 ppt [53]) shows that the integrated brightness temperature for the marine ice case will increase by about 5 K for the vertical polarization and 1 K or less for the horizontal polarization relative to the marine ice-free case [61]. However, the irregular melt freeze patterns described in [8] and [54] are not consistent with the more regular T_B patterns observed.

Another possibility is that the emission is primarily associated with shallower depths in the ice column. We assess T_B sensitivity to the ice temperature at depth by making the simplifying assumption that the ice temperature profile at each SMAP pixel varies linearly from the ERA5 surface skin temperature and the sea temperature fixed at -1.8°C . We calculate the physical temperature at the same depth for each of the SMAP pixels and compare that physical temperature to the measured T_B . Fig. 16 shows SMAP T_B^v compared to the ice temperature at 294 m in depth, where the highest correlation between T_B^v and estimated temperature is obtained (Pearson correlation coefficient of 0.74, p -value < 0.05). T_B^v and the ice temperature at depth are reasonably correlated with a maximum correlation (correlation coefficient > 0.60) between 100–400 m in depth.

The correlation decreases for thicknesses greater than 400 m and becomes insignificant (p -value > 0.05) below 700 m in depth. This suggests that T_B^v at L-band over the RIS is sensitive to about the first 400–500 m of ice and not very sensitive to the properties of deeper ice in the column. This is consistent with estimates of the temperature-dependent absorption coefficient which increases with temperature [62]. Increasing absorption limits penetration along the optical path at L-band to less than 550 m for an ice shelf temperature of -27°C and about 250 m for an average temperature of -14°C . The reduced effective ice thicknesses of about 513 and 233 m, respectively, are computed by multiplying the penetration depth by the cosine of the propagation angle in ice ($\sim 21^\circ$) corresponding to the refracted SMAP viewing angle. For comparison, the penetration depth at L-band is almost doubled on the East Antarctic Plateau [18] where surface temperatures are about 218 K at Dome C [63].

Our analysis plausibly explains why T_B warms for thinner ice, although the large dispersion observed in Fig. 16 suggests that other processes are involved. Surface temperature is a boundary condition on the physical temperature profile but is slowly varying spatially (Fig. 2). Snow accumulation grows from 100 to 140 mm/yr west to east and 100 to 180 mm/yr south to north [42] which changes the rate of downward advection of colder ice. Both processes along with changes

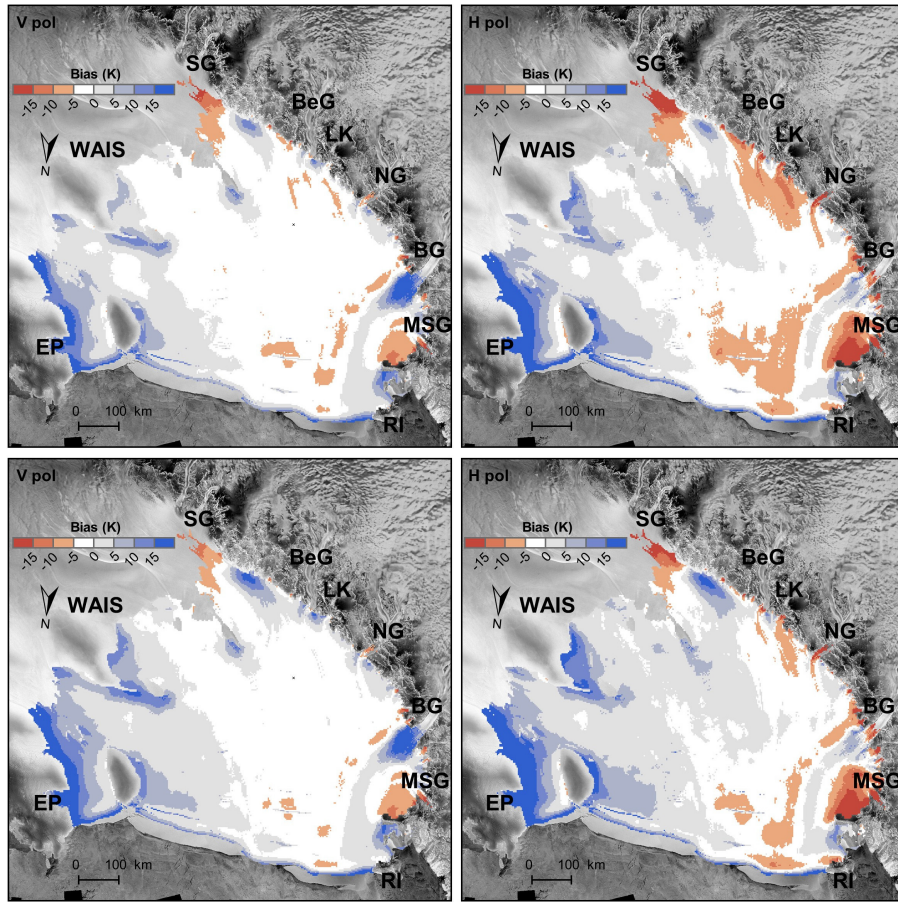


Fig. 15. Difference between T_B based on linear regression analysis and measured T_B and T_B based on linear regression analysis of scatter plots. (Top) Results for a period of 6 days in April 2015 and prior to the major 2016 melt event. (Bottom) Results when the April regression parameters are applied to the multiyear data set.

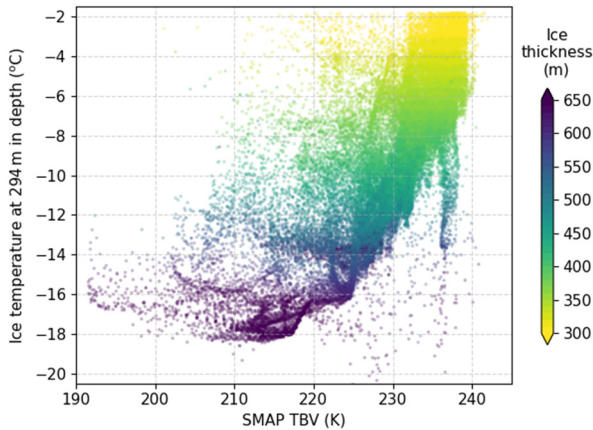


Fig. 16. SMAP T_B^v compared to the ice temperature at 294-m depth over RIS. Ice thickness of each pixel is color coded.

in oceanic heat flux limit the applicability of the linear temperature model.

VIII. CONCLUSION

We have shown that SMAP T_B and backscatter data are coupled to glaciological processes typical of the RIS.

Scattering from ice lenses and layers formed when melt refreezes in the firn increase scattering and decrease T_B . Cold outflow from the interior East and West Antarctic results in wide, cool T_B plumes correlated with the ice streams and narrow cool bands correlated with Transantarctic outlet glaciers. Although the presence of marine ice accretion to the base of the ice is expected to warm the net emission, we do not see systematic evidence for spatial distributions of marine ice in the data.

We find that T_B is negatively correlated with ice thickness which contrasts with the positive correlation observed on the interior ice sheet where the ice is much thicker (>1000 m) and colder. Based on a simplified functional form of the physical temperature profile, we conclude that the temperature-dependent penetration depth into the warm shelf ice limits the sensitivity of the L-band T_B signal to depths shallower than 400–500 m. One approach to overcoming the depth limitation is to lower the frequency range and increase the frequency bandwidth. Both the technology and scientific benefit of a wideband approach have been demonstrated during airborne experiments in the Arctic and Antarctic [23] and are prime considerations for developing new concepts for spaceborne radiometer systems [64].

REFERENCES

- [1] R. H. Thomas, "The creep of ice shelves theory," *J. Glaciol.*, vol. 12, no. 64, pp. 45–53, 1973.
- [2] S. Wang et al., "Controls on Larsen C ice shelf retreat from a 60-year satellite data record," *J. Geophys. Res., Earth Surf.*, vol. 127, Mar. 2022, Art. no. e2021JF006346.
- [3] J. Weertman, "Stability of the junction of an ice sheet and an ice shelf," *J. Glaciol.*, vol. 13, no. 67, pp. 3–11, 1974.
- [4] G. R. Lange, "Deep rotary core drilling in ice," CRREL, Hanover, NH, USA, Tech. Rep., 94, 1973.
- [5] C. R. Bentley and K. C. Jezek, "RISS, RISP and RIGGS: Post-IGY glaciological investigations of the Ross Ice Shelf in the U.S. Programme," *J. Roy. Soc. New Zealand*, vol. 11, no. 4, pp. 355–372, Dec. 1981.
- [6] J. W. Clough and B. L. Hansen, "The Ross Ice Shelf project," *Science*, vol. 203, no. 4379, pp. 433–434, Feb. 1979.
- [7] C. Stevens et al., "Ocean mixing and heat transport processes observed under the Ross Ice Shelf control basal melt," *PNAS*, vol. 117, no. 29, pp. 16799–16804, 2020.
- [8] I. Das, "Multidecadal basal melt rates and structure of the Ross Ice Shelf, Antarctica, using airborne ice penetrating radar," *J. Geophys. Res., Earth Surf.*, vol. 125, Mar. 2020, Art. no. e2019JF005241.
- [9] P. Fretwell et al., "Bedmap2: Improved ice bed, surface and thickness datasets for Antarctica," *Cryosphere*, vol. 7, no. 2, pp. 375–393, 2013.
- [10] M. Morlighem, "Deep glacial troughs and stabilizing ridges unveiled beneath the margins of the Antarctic ice sheet," *Nature Geosci.*, vol. 13, no. 2, pp. 132–137, 2020.
- [11] K. C. Jezek, "Observing the Antarctic ice sheet using the RADARSAT-1 synthetic aperture radar," *Polar Geogr.*, vol. 27, no. 3, pp. 197–209, Jul. 2003.
- [12] E. Rignot, J. Mouginot, and B. Scheuchl, "Ice flow of the Antarctic ice sheet," *Science*, vol. 333, no. 6048, pp. 1427–1430, Sep. 2011.
- [13] E. Rignot, J. Mouginot, and B. Scheuchl, "Antarctic grounding line mapping from differential satellite radar interferometry," *Geophys. Res. Lett.*, vol. 38, no. 10, May 2011, Art. no. L10504.
- [14] H. J. Zwally, J. W. Robbins, S. B. Luthcke, B. D. Loomis, and F. Rémy, "Mass balance of the Antarctic ice sheet 1992–2016: Reconciling results from GRACE gravimetry with ICESat, ERS1/2 and ENVISAT altimetry," *J. Glaciol.*, vol. 67, no. 263, pp. 533–559, Jun. 2021.
- [15] H. Liu and L. Wang, "Spatio-temporal variations of snow melt zones in Antarctic ice sheet derived from satellite SMMR and SSM/I data (1978–2004)," *J. Geophys. Res.*, vol. 111, Jan. 2006, Art. no. F01003.
- [16] L. D. Trusel, K. E. Frey, S. B. Das, P. K. Munneke, and M. R. van den Broeke, "Satellite-based estimates of Antarctic surface meltwater fluxes," *Geophys. Res. Lett.*, vol. 40, no. 23, pp. 6148–6153, Dec. 2013.
- [17] K. Jezek, "Radiometric approach for estimating relative changes in interglacial average temperature," *IEEE Trans. Geosci. Remote Sens.*, vol. 53, no. 1, pp. 134–143, Jan. 2015.
- [18] G. Macelloni, M. Leduc-Leballeur, F. Montomoli, M. Brogioni, C. Ritz, and G. Picard, "On the retrieval of internal temperature of Antarctica ice sheet by using SMOS observations," *Remote Sens. Environ.*, vol. 233, Nov. 2019, Art. no. 111405.
- [19] M. Leduc-Leballeur, G. Picard, G. Macelloni, A. Mialon, and Y. H. Kerr, "Melt in Antarctica derived from Soil Moisture and Ocean Salinity (SMOS) observations at L band," *Cryosphere*, vol. 14, no. 2, pp. 539–548, Feb. 2020.
- [20] J. Z. Miller, R. Culberg, D. G. Long, C. A. Shuman, D. M. Schroeder, and M. J. Brodzik, "An empirical algorithm to map perennial firn aquifers and ice slabs within the Greenland ice sheet using satellite L-band microwave radiometry," *Cryosphere*, vol. 16, no. 1, pp. 103–125, Jan. 2022.
- [21] J. Z. Miller, D. G. Long, C. A. Shuman, R. Culberg, M. Hardman, and M. J. Brodzik, "Mapping firn saturation over Greenland using NASA's soil moisture active passive satellite," *IEEE J. Sel. Topics Appl. Earth Observ. Remote Sens.*, vol. 15, pp. 3714–3729, 2022.
- [22] T. Scambos et al., "Antarctic ice shelf aquifers: Characteristics and potential contributions to ice shelf loss," in *Proc. EGU Gen. Assem.*, Vienna, Austria, May 2022, Paper EGU22-820, doi: 10.5194/egusphere-egu22-820.
- [23] J. T. Johnson et al., "Microwave radiometry at frequencies from 500 to 1400 MHz: An emerging technology for Earth observations," *IEEE J. Sel. Topics Appl. Earth Observ. Remote Sens.*, vol. 14, pp. 4894–4914, 2021.
- [24] C. Yardim, "Greenland ice sheet subsurface temperature estimation using ultrawideband microwave radiometry," *IEEE Trans. Geosci. Remote Sens.*, vol. 60, pp. 1–12, 2022.
- [25] M. Brogioni, L.-L. M. M. J. Andrews, G. Macelloni, J. T. Johnson, K. C. Jezek, and C. Yardim, "500–2000-MHz airborne brightness temperature measurements over the East Antarctic plateau," *IEEE Geosci. Remote Sens. Lett.*, vol. 19, pp. 1–5, 2022.
- [26] M. Brogioni, "Ice sheet and sea ice ultrawideband microwave airborne experiment (ISSIUMAX) in Antarctica: First results from Terra Nova Bay," *Cryosphere*, vol. 2022, pp. 1–35, Jan. 2022.
- [27] K. C. Jezek, C. Yardim, J. T. Johnson, G. Macelloni, and M. Brogioni, "Analysis of ice-sheet temperature profiles from low-frequency airborne remote sensing," *J. Glaciol.*, vol. 2022, pp. 1–11, Mar. 2022.
- [28] D. Entekhabi et al., "The soil moisture active passive (SMAP) mission," *Proc. IEEE*, vol. 98, no. 5, pp. 704–716, May 2010.
- [29] D. G. Long, M. J. Brodzik, and M. A. Hardman, "Enhanced-resolution SMAP brightness temperature image products," *IEEE Trans. Geosci. Remote Sens.*, vol. 57, no. 7, pp. 4151–4163, Jul. 2019.
- [30] D. G. Long, M. J. Brodzik, and M. A. Hardman, "The effective resolution of CETB image products," NSIDC, Boulder, CO, USA, Tech. Rep., 21, 2021.
- [31] M. J. Brodzik, D. G. Long, and M. A. Hardman, "SMAP radiometer twice-daily rSIR-enhanced EASE grid 2.0 brightness temperatures, version 1," NASA Nat. Snow Ice Data Center Distrib. Act. Arch. Center, Boulder, CO, USA, 2019. Accessed: Jun. 1, 2022.
- [32] R. West, "Soil moisture active passive (SMAP) L1B_S0, L1C_S0, algorithm theoretical basis document (ATBD)," Jet Propulsion Lab., Pasadena, CA, USA, 2014, p. 70. [Online]. Available: <https://www.frames.gov/catalog/20014>
- [33] D. G. Long and J. Z. Miller, "Validation of the effective resolution of SMAP enhanced resolution backscatter products," *IEEE J. Sel. Topics Earth Observ. Remote Sens.*, 2022.
- [34] J. Z. Miller, D. G. Long, M. J. Brodzik, and M. A. Hardman, "SMAP enhanced-resolution scatterometer and synthetic aperture radar image products," in *Proc. IEEE Int. Geosci. Remote Sens. Symp. (IGARSS)*, 2022, pp. 4300–4303, doi: 10.1109/IGARSS46834.2022.9884939.
- [35] D. G. Long and M. R. Drinkwater, "Azimuth variation in microwave scatterometer and radiometer data over Antarctica," *IEEE Trans. Geosci. Remote Sens.*, vol. 38, no. 4, pp. 1857–1870, Jul. 2000.
- [36] R. D. Lindsley and D. G. Long, "ASCAT and QuikSCAT azimuth modulation of backscatter over East Antarctica," *IEEE Geosci. Remote Sens. Lett.*, vol. 13, no. 8, pp. 1134–1138, Aug. 2016.
- [37] D. G. Long and J. Z. Miller, "SMAP radar SAR and SIR-enhanced twice-daily EASE-grid 2.0 radar backscatter," NASA Nat. Snow Ice Data Center Distrib. Act. Arch. Center, Boulder, CO, USA, 2022. Accessed: Jun. 1, 2022.
- [38] M. J. Brodzik, B. Billingsley, T. Haran, B. Raup, and M. H. Savoie, "EASE-Grid 2.0: Incremental but significant improvements for Earth-gridded data sets," *ISPRS Int. J. Geo-Inf.*, vol. 1, no. 1, pp. 32–45, 2012.
- [39] M. J. Brodzik, B. Billingsley, T. Haran, B. Raup, and M. H. Savoie, "EASE-Grid 2.0: Incremental but significant improvements for Earth-Gridded data sets," *ISPRS Int. J. Geo-Inf.*, vol. 1, no. 1, pp. 32–45, 2012.
- [40] C. R. Bentley, J. W. Clough, K. C. Jezek, and S. Shabtaie, "Ice-thickness patterns and the dynamics of the Ross Ice Shelf, Antarctica," *J. Glaciol.*, vol. 24, no. 90, pp. 287–294, 1979.
- [41] R. H. Ragle, B. L. Hansen, A. J. Gow, and R. W. Patenaude, "Deep core drilling in the Ross Ice Shelf, little America V, Antarctica," U.S. Army Snow Ice and Permafrost Research Establishment, Wilmette, IL, USA, Tech. Rep. 70, 1960.
- [42] R. H. Thomas, D. R. MacAyeal, D. H. Eilers, and D. R. Gaylor, "Glaciological studies on the Ross Ice Shelf, Antarctica, 1973–1978," *Ross Ice Shelf: Glaciol. Geophys.* vol. 42, pp. 21–53, Jan. 1984.
- [43] H. B. Clausen, W. Dansgaard, J. Nielsen, and J. W. Clough, "Surface accumulation on the Ross Ice Shelf," *Antarctic J. United States*, vol. 5, no. 5, pp. 68–72, 1979.
- [44] C. S. Neal, "The dynamics of the Ross Ice Shelf revealed by radio echo-sounding," *J. Glaciol.*, vol. 24, no. 90, pp. 295–307, 1979.
- [45] K. C. Jezek, "Recent changes in the dynamic condition of the Ross Ice Shelf, Antarctica," *J. Geophys. Res.*, vol. 889, no. B1, pp. 409–416, 1984.
- [46] K. C. Jezek, C. R. Bentley, and J. W. Clough, "Electromagnetic sounding of bottom crevasses on the Ross Ice Shelf, Antarctica," *J. Glaciol.*, vol. 24, no. 90, pp. 321–330, 1979.

- [47] A. J. Gow, "Deep core studies of the accumulation and densification of snow at Byrd station and little America V, Antarctica," U.S. Army Cold Regions Research and Engineering Laboratory, Hanover, NH, USA, Tech. Rep., 197, 1968.
- [48] A. P. Crary, "Glaciological regime at little America station, Antarctica," *J. Geophys. Res.*, vol. 66, no. 3, pp. 871–878, Mar. 1961.
- [49] A. P. Crary and W. H. Chapman, "Additional glaciological measurements at the abandoned little America station, Antarctica," *J. Geophys. Res.*, vol. 68, no. 21, pp. 6064–6065, Nov. 1963.
- [50] J. H. Rand, "100-meter ice cores from the South Pole and the Ross Ice Shelf," *Antarctic J. United States*, vol. 15, p. 154, Jul. 1975.
- [51] J. W. Clough, "J-9 drill hole temperatures," U.S. Antarctic Program (USAP) Data Center, 2020, doi: [10.15784/601316](https://doi.org/10.15784/601316).
- [52] D. R. MacAyeal and R. H. Thomas, "Ross Ice Shelf temperatures support a history of ice-shelf thickening," *Nature*, vol. 282, no. 5740, pp. 703–705, Dec. 1979.
- [53] I. A. Zotikov, V. S. Zagorodnov, and J. V. Raikovsky, "Core drilling through the Ross Ice Shelf (Antarctica) confirmed basal freezing," *Science*, vol. 207, no. 4438, pp. 1463–1465, Mar. 1980.
- [54] G. Moholdt, L. Padman, and H. A. Fricker, "Basal mass budget of Ross and Filchner–Ronne ice shelves, Antarctica, derived from Lagrangian analysis of ICESat altimetry," *J. Geophys. Res., Earth Surf.*, vol. 119, no. 11, pp. 2361–2380, Nov. 2014.
- [55] S. Tan et al., "Physical models of layered polar firn brightness temperatures from 0.5 GHz to 2 GHz," *IEEE J. Sel. Topics Appl. Earth Observ. Remote Sens.*, vol. 8, no. 7, pp. 3681–3691, Jul. 2015.
- [56] K. C. Jezek et al., "500–2000 MHz brightness-temperature spectra of the Northwestern Greenland ice sheet," *IEEE Trans. Geosci. Remote Sens.*, vol. 56, no. 3, pp. 1485–1496, Mar. 2018.
- [57] O. Torinesi, M. Fily, and C. Genthon, "Variability and trends of the summer melt period of Antarctic ice margins since 1980 from microwave sensors," *J. Climate*, vol. 16, no. 7, pp. 1047–1060, Apr. 2003.
- [58] J. P. Nicholas et al., "January 2016 extensive summer melt in West Antarctica favoured by strong El Niño," *Nature Commun.*, vol. 8, no. 2, pp. 1–10, 2017.
- [59] J. Zeng, P. Shi, K.-S. Chen, H. Ma, H. Bi, and C. Cui, "On the relationship between radar backscatter and radiometer brightness temperature from SMAP," *IEEE Trans. Geosci. Remote Sens.*, vol. 60, pp. 1–16, 2022.
- [60] M. Pablos, M. Piles, V. González-Gambau, A. Camps, and M. Vall-Ilossera, "Ice thickness effects on a quarius brightness temperatures over Antarctica," *J. Geophys. Res., Oceans*, vol. 120, no. 4, pp. 2856–2868, Apr. 2015.
- [61] M. Brogioni et al., "Modeling low frequency microwave emission from Antarctic ice shelves," *Trans. Geosci. Remote Sens.*, to be published.
- [62] C. Matzler, "Microwave dielectric properties of ice," in *Thermal Microwave Radiation: Applications for Remote Sensing* (Electromagnetic Waves Series), vol. 52, C. Matzler, P. Rosenkranz, A. Battaglia, and J. Wigeron, Eds. Edison, NJ, USA: IET, 2006, pp. 455–462.
- [63] C. Ritz, L. Llibouty, and C. Rado, "Analysis of a 870 m deep temperature profile at Dome C," *Ann. Glaciol.*, vol. 3, pp. 284–289, Jan. 1982.
- [64] G. Macelloni et al., "Cryorad: A low-frequency wideband radiometer mission for the study of the Cryosphere," in *Proc. IEEE Int. Geosci. Remote Sens. Symp.*, Valencia, Spain, Jul. 2018, pp. 1998–2000.



Kenneth C. Jezek received the B.S. degree in physics from the University of Illinois Urbana-Champaign, Champaign, IL, USA, in 1973, and the M.S. and Ph.D. degrees in geophysics from the University of Wisconsin–Madison, Madison, WI, USA, in 1977 and 1980, respectively.

Before joining the Byrd Polar Research Center, The Ohio State University (OSU), Columbus, OH, USA, as the Director, in 1989, he was a Geophysicist with the U.S. Army Cold Regions Research and Engineering Laboratory, Hanover, NH, USA. He is currently a Professor Emeritus with the Byrd Polar and Climate Research Center, School of Earth Sciences, OSU. His research interests include the application of ultra-wideband radiometry to ice sheets and sea ice studies.



Shujie Wang received the B.S. degree in geographic information systems and the M.S. degree in cartography and geographic information science from Sun Yat-sen University, Guangzhou, China, in 2010 and 2012, respectively, and the Ph.D. degree in geography from the University of Cincinnati, Cincinnati, OH, USA, in 2018.

She was a Post-Doctoral Research Scientist with the Lamont-Doherty Earth Observatory, Columbia University, Palisades, NY, USA, from 2018 to 2020. She is currently an Assistant Professor with the Department of Geography, The Pennsylvania State University, University Park, PA, USA. Her research interests include ice sheet processes, remote sensing, machine learning, and numerical modeling.

Marion Leduc-Leballeur received the M.Sc. degree in remote sensing and the Ph.D. degree in atmospheric physics from Sorbonne University, Paris, France, in 2008 and 2012, respectively.

She was with the Laboratoire Atmosphères, Milieux, Observations Spatiales (LATMOS), Institut Pierre Simon Laplace (IPSL), Paris. From 2012 to 2016, she was with the IGE, Grenoble, France. Since 2017, she has been with the Institute of Applied Physics Nello Carrara (IFAC), Italian National Research Center (CNR), Florence, Italy. Her research interests include snow properties from microwave remote sensing, using electromagnetic modeling, satellite observations, and in situ measurements.



Joel T. Johnson (Fellow, IEEE) received the bachelor's degree in electrical engineering degree from the Georgia Institute of Technology, Atlanta, GA, USA, in 1991, and the S.M. and Ph.D. degrees from the Massachusetts Institute of Technology, Cambridge, MA, USA, in 1993 and 1996, respectively.

He is currently the Burn and Sue Lin Professor with the Department of Electrical and Computer Engineering and ElectroScience Laboratory, The Ohio State University, Columbus, OH, USA. His research interests include microwave remote sensing, propagation, and electromagnetic wave theory.

Dr. Johnson is a member of the Commissions B and F of the International Union of Radio Science (URSI) and a member of Tau Beta Pi, Eta Kappa Nu, and Phi Kappa Phi. He received the 1993 Best Paper Award from the IEEE Geoscience and Remote Sensing Society, was named an Office of Naval Research Young Investigator, National Science Foundation Career Awardee, and PECASE Award recipient in 1997, and was recognized by the U.S. National Committee of URSI as a Booker Fellow in 2002.



Marco Brogioni (Member, IEEE) was born in Siena, Italy, in 1976. He received the M.Sc. degree in telecommunications engineering from the University of Siena, Siena, Italy, in 2003, and the Ph.D. degree in remote sensing from the University of Pisa, Pisa, Italy, in 2008.

Since 2004, he has been with the Microwave Remote Sensing Group, Institute of Applied Physics Nello Carrara (IFAC), Consiglio Nazionale delle Ricerche (CNR), Florence, Italy. From 2006 to 2007, he has been a Visiting Student with the University of California at Santa Barbara, Santa Barbara, CA, USA. He is currently involved in several international projects regarding polar regions. He is also involved in the design and manufacturing of microwave radiometers (L- to Ka-bands). His research interests include passive and active microwave remote sensing applied to snow by using satellite and ground-based data, especially the development of electromagnetic models for passive and active microwave remote sensing of snow, vegetation, and soil.

Dr. Brogioni was a recipient of the Third Prize at the URSI GA Student Prize Paper Competition in Chicago, IL, USA, in 2008. He served as the Chair for the 16th MicroRad 2020 virtual meeting and in the local organizing committee of the 10th Microrad, Florence, in 2008 and the Microwave Signature Symposium of the URSI Commission-F, Florence, in 2010. He participated in the Italian Antarctic Expeditions, carrying out his research at Concordia Station (Dome-C) and Mario Zucchelli Station (Ross Sea) in 2013, 2015, and 2018, respectively.



Julie Z. Miller received the B.S. degree in applied mathematics and the M.S. and Ph.D. degrees in geography from the University of Utah, Salt Lake City, UT, USA, in 2010, 2012, and 2019, respectively, with a focus on microwave remote sensing of polar ice sheets.

She is currently a Research Scientist with The Earth Science and Observation Center, Cooperative Institute for Research in Environmental Sciences (CIRES), University of Colorado, Boulder, CO, USA. She is also a member of NASA's SMAP Science Team. She has participated in field and airborne campaigns in both Greenland and Antarctica. Her research interests include developing algorithms to map surface and subsurface meltwater in Greenland and Antarctica using multifrequency microwave radiometers and radar scatterometer imagery.

Dr. Miller completed a Post-Doctoral Fellowship at the Byrd Polar and Climate Research Center, The Ohio State University, Columbus, OH, USA.



David G. Long (Fellow, IEEE) received the Ph.D. degree in electrical engineering from the University of Southern California, Los Angeles, CA, USA, in 1989.

From 1983 to 1990, he was with NASA's Jet Propulsion Laboratory (JPL), Pasadena, CA, USA, where he developed advanced radar remote sensing systems. While at JPL, he was the Project Engineer on the NASA Scatterometer (NSCAT) Project which flew from 1996 to 1997. He also managed the SCANSAT project, the precursor to SeaWinds which was flown in 1999 on QuikSCAT, in 2002 on ADEOS-II, and in 2014 on the International Space Station. He is currently a Professor with the Electrical and Computer Engineering Department, Brigham Young University (BYU), Provo, UT, USA, where he teaches upper division and graduate courses in communications, microwave remote sensing, radar, and signal processing and is also the Director of the BYU Center for Remote Sensing. He is the Principal Investigator on several NASA-sponsored research projects in remote sensing. He has over 400 publications in various areas including signal processing, radar scatterometry, and synthetic aperture radar. His research interests include microwave remote sensing, radar theory, space-based sensing, estimation theory, signal processing, and mesoscale atmospheric dynamics.

Dr. Long received the NASA Certificate of Recognition several times and is an Associate Editor of IEEE GEOSCIENCE AND REMOTE SENSING LETTERS.



Giovanni Macelloni (Senior Member, IEEE) received the M.Sc. degree in electronic engineering from the University of Florence, Florence, Italy, in 1993.

Since 1995, he has been with the Institute of Applied Physics-CNR-Florence, Florence, where is currently the Head of Research. Since 2019, he has been an Adjunct Professor with the University of Venice, Venice, Italy. He is also involved in the design and development of microwave remote sensing systems both from the ground, the air, and satellites. The research has been carried out in the framework of several national and international programs granted by Italian Entities, the European community, and Space Agencies (ESA, ASI, NASA, and JAXA) and includes the participation in international teams for the studying of the cryosphere and the development and assessment of future space-borne missions. His research interests include microwave active and passive remote sensing for the study of the Earth system and cryosphere in particular.

Dr. Macelloni is a member of the Cryonet Team of Global CryosphereWatch of the WMO, the Italian Scientific Antarctic Commission which implements the National Antarctic Programme, and is the Italian National delegate at the Scientific Committee of Antarctic Research. He was a Tutor of Ph.D. students, was a reviewer for several international committees, organizations, and international journals, and acted as an Organizer and Co-Chair of international conferences. He is currently an Associate Editor of the IEEE TRANSACTIONS ON GEOSCIENCE AND REMOTE SENSING.